ELSEVIER

# On the computation of multi-material flows using ALE formulation

Hong Luo [a,*], Joseph D. Baum [a], Rainald Löhner [b]

[a] *Center for Applied Computational Sciences, Science Applications International Corporation, 1710 SAIC Drive, MS 2-6-9, McLean, VA 22102, USA*
[b] *Institute for Computational Sciences and Informatics, George Mason University, Fairfax, VA 22030, USA*

## Abstract

Computation of compressible multi-fluid flows with a general equation of state using interface tracking and moving grid approach is discussed in this paper. The AUSM+, HLLC, and Godunov methods are presented and implemented in the context of arbitrary Lagrangian–Eulerian formulation for solving the unsteady compressible Euler equations. The developed methods are fully conservative, and used to compute a variety of multi-component flow problems, where the equations of state can be drastically different and stiff. Numerical results indicate that both ALE HLLC and Godunov schemes demonstrate their simplicity and robustness for solving such multi-phase flow problems, and yet ALE AUSM+ scheme exhibits strong oscillations around material interfaces even using a first order monotone scheme and therefore is not suitable for this class of problems.
© 2003 Elsevier B.V. All rights reserved.

## 1. Introduction

Multi-material flows, where a moving interface exists between two immiscible fluids, can be found in a variety of engineering problems. Development of numerically accurate and computationally efficient algorithms for multi-material flow simulations remains one of the unresolved issues in computational fluid dynamics. These flow problems are characterized by the existence of material interfaces. The modeling of these complicated free boundaries poses a difficult numerical challenge, as they are either time dependent or unknown a priori and determined as part of the solution. A number of numerical methods exist for solving the interface problems: interface capturing methods (mixed cell methods) [5–9], level set methods [23,24], volume of fluid and interface reconstruction methods [22], interface tracking methods [1–4,25], free-Lagrange methods [26]. Unfortunately, there are still limitations and shortcomings attached to each of them. In

---

[*] Corresponding author. Tel.: +1-703-676-5957; fax: +1-703-676-5323.
*E-mail address:* hong.luo@saic.com (H. Luo).

general, for all these methods that allow mixed cells, the computation of thermodynamical variables such as pressure, speed of sound, and temperature on mixed cells is difficult to achieve correctly. In particular, when the equations of state for different materials are drastically different, a small error on the thermodynamical variables can lead to collapse or meaningless of the computation. For all these methods where the interface is represented and tracked explicitly either by marking it with special marker points, or by treating it like a boundary, it is difficulty to handle very complex free surface problems, especially those involving interface topological changes such as merging or breakup of the interface.

The objective of the research presented in this paper is to develop a numerical method for the computation of compressible multi-material flow problems using the interface tracking approach. The development of such numerical method is strongly motivated by the need to model underwater explosions. Simulation of underwater explosions plays an important role in determining and assessing platform vulnerability and weapon lethality. Such task requires accurate prediction of target loading, which primarily occurs as a result of the initial shock wave and subsequent bubble collapse. Numerical simulation of underwater explosions represents a technical challenge, as it involves modeling several complex physical processes: the propagation of the detonation wave through the high explosive; the expansion of the primary shock wave into water; the pulsating behavior of the gas bubble; and the interaction of these shocks with the near-by structure. These processes occur over vastly different time scales, from microseconds for the detonation wave, to millisecond for the propagation of the shock in water, to second for bubble pulsation, making 3D explicit Euler simulations expensive, if not impossible to model numerically at present.

In this paper, the computation of compressible multi-material flow problems is discussed using the interface tracking approach where the surface separating different materials is explicitly tracked as a Lagrangian surface. The arbitrary Lagrangian–Eulerian (ALE) formulation in conjunction with an appropriate equation of state for each material is used to solve the resulting equations on a moving grid. Only those methods which can easily and simply accommodate general equations of state for real fluids can be considered to solve this class of flow problems, which feature the existence of different equations of state, which can be general, stiff, and in tabular form. Although a number of characteristics-based upwind methods have been developed for solving compressible Euler equations in Eulerian formulation, their accuracy and robustness for solving compressible Euler equations in ALE formulation are relatively unexplored. In this work, the ALE formulation of AUSM+ [10], HLLC [11], and the approximate Riemann Solver of Colella [12] has been described and implemented. The developed methods have been used for computing a variety of multi-material interface problems, including an underwater explosion problem. Numerical results indicate that even the first order ALE AUSM+ scheme experiences deficiencies: exhibit oscillations around the material interface and lead to the collapse of calculation for the underwater explosion problem. On the other hand, both ALE HLLC and Godunov schemes are found to be able to offer accurate and robust solutions for capturing strong shock, contact, and phase discontinuities on arbitrarily moving grids.

The outline of this paper is as follows: In Section 2 the governing equations in the context of ALE formulation are described. The geometric conservation law is then presented in Section 3. The ALE formulation of AUSM+, HLLC, and Godunov schemes is described in Section 4. The results of our calculations for a variety of multi-material flow problems and the comparison of numerical solutions with available analytical solutions and experimental data are presented in Section 5. Finally, the conclusions are summarized in Section 6.

## 2. Governing equations

The unsteady compressible Euler equations for a moving control volume can be expressed in integral form as

$$\frac{\partial}{\partial t}\int_{\Omega(t)}\mathbf{U}\,d\Omega + \int_{\Gamma(t)}\mathbf{F}\,d\Gamma = 0, \tag{2.1}$$

where $\Omega(t)$ is the moving control volume, and $\Gamma(t)$ its boundary. The flow variable vector $\mathbf{U}$ and the inviscid flux vector $\mathbf{F}$ are defined by

$$\mathbf{U}=\begin{pmatrix}\rho\\\rho\mathbf{v}\\\rho E\end{pmatrix},\qquad \mathbf{F}=\begin{pmatrix}(\mathbf{v}-\dot{\mathbf{x}})\cdot\mathbf{n}\rho\\(\mathbf{v}-\dot{\mathbf{x}})\cdot\mathbf{n}\rho\mathbf{v}+p\mathbf{n}\\(\mathbf{v}-\dot{\mathbf{x}})\cdot\mathbf{n}\rho E+p\mathbf{v}\cdot\mathbf{n}\end{pmatrix}, \tag{2.2}$$

where $\rho$, $p$, and $E$ are the density, pressure, and specific total energy of the fluid, respectively, and $\mathbf{v}$ is the velocity vector of the flow. $\mathbf{n}$ denotes the unit outward normal vector to the moving boundary $\Gamma(t)$, whose velocity is denoted by $\dot{\mathbf{x}}$. In the following, $\mathbf{u}$ is used to denote the fluid velocity relative to the interface velocity, i.e.,

$$\mathbf{u}=\mathbf{v}-\dot{\mathbf{x}}. \tag{2.3}$$

When $\dot{\mathbf{x}}=0$, the system (2.1) and (2.2) corresponds to the Eulerian description of the conservation, whereas $\dot{\mathbf{x}}=\mathbf{v}$ results in the Lagrangian description of the conservation, where the control volume moves with the instantaneous fluid velocity. Because of the generality, or in other words, arbitrariness of the description offered by Eqs. (2.1) and (2.2), the system (2.1) and (2.2) is often referred to as the ALE form of the conservation laws.

This set of equations is completed by the addition of an equation of state (EOS) which establishes the relationship between, at most, three thermodynamic variables. Here the EOS is taken to be of the form

$$p=p(\rho,e), \tag{2.4}$$

where the specific internal energy, $e$, is related to the specific total energy by

$$E=e+\frac{|\mathbf{v}|^2}{2}. \tag{2.5}$$

Introducing the entropy, $s$, the speed of sound, $c$, is defined by

$$c^2\equiv\left.\frac{dp(\rho,s)}{d\rho}\right|_s=\frac{\partial p}{\partial e}\frac{p}{\rho^2}+\frac{\partial p}{\partial\rho}, \tag{2.6}$$

where the partial derivatives on the right in Eq. (2.6) are with respect to the function $p=p(\rho,e)$.

## 3. Geometric conservation law

When grids are moving and/or deforming, the conservation property may be violated unless the following geometric conservation law (GCL) is satisfied

$$\frac{\partial\Omega}{\partial t}-\int_{\Gamma(t)}\dot{\mathbf{x}}\cdot\mathbf{n}\,d\Gamma = 0. \tag{3.1}$$

The GCL can be easily derived by assuming uniform velocity and density fields in the continuity equation. Clearly, GCL will ensure free stream capturing with moving and/or deforming grids. The GCL may be satisfied by either explicitly updating the volume $\Omega(t)$ through an evaluation of Eq. (3.1) or implicitly defining the control surface area $\Gamma(t)$ as a weighted average of the $n$ and $n+1$ time level areas such that

Eq. (3.1) is satisfied automatically by construction. Geometrically conservative formulas for a general polygons and polyhedra used in finite volume schemes can be found in Zhang et al. [13] and Nkonga et al. [14]. A more general treatment of the GCL is presented by Lesoinne et al. [15], which recovers the time-averaged normal formulas for polygons and polyhedra derived in [13,14].

## 4. Numerical methods

The governing equation (2.1) is discretized using a finite volume cell-vertex formulation, where the cell-averaged variables are stored at the vertices of the grid. The control volumes are non-overlapping dual cells which are constructed by the median faces of the tetrahedra in 3D and the triangle in 2D. The finite volume approximation of the governing equation (2.1), applied to the control volume around a node $i$ becomes

$$\frac{\mathrm{d}(\Omega \mathbf{U})_i}{\mathrm{d}t} + \int_{\Gamma_i} \mathbf{F} \, \mathrm{d}\Gamma = 0, \tag{4.1}$$

where $\Gamma_i$ is the boundary of the control volume $\Omega_i$. The flux integral in Eq. (4.1) is evaluated by summing all the contributions over the cell interfaces between the node $i$ and its neighboring node $j$, $\Gamma_{ij}(= \Gamma_i \cap \Gamma_j)$. Eq. (4.1) can then be rewritten in a compact form as

$$\frac{\mathrm{d}(\Omega \mathbf{U})_i}{\mathrm{d}t} = \mathbf{R}_i, \tag{4.2}$$

where $\mathbf{R}_i$ is the right hand side residual,

$$\mathbf{R}_i = -\sum_j \int_{\Gamma_{ij}} \mathbf{F} \, \mathrm{d}\Gamma. \tag{4.3}$$

The numerical fluxes on the interface $\Gamma_{ij}$ are approximated at the mid-edge of the edge $ij$, and the integral along the interface can then be evaluated as

$$\int_{\Gamma_{ij}} \mathbf{F} \cdot \mathbf{n} \, \mathrm{d}\Gamma = \mathbf{F}_{ij} \Gamma_{ij}, \tag{4.4}$$

where $\Gamma_{ij}$ denotes the magnitude of the interface.

Over the last two decades characteristic-based upwind methods have established themselves as the methods of choice for prescribing the numerical fluxes for compressible Euler equations. However, many popular and enduring methods such as Roe's flux-difference scheme [16] and van Leer's flux-vector scheme [17] cannot be easily modified to solve the compressible Euler equations with a general EOS, as they are primarily derived under the assumption of ideal gas EOS. The three methods considered here, AUSM+ [10], HLLC [11], and approximate Godunov [12] share the same feature that they all can easily and simply accommodate general EOS: a necessary requirement for the problems to be solved. Although the three upwind schemes have been proven to be accurate, simple, and robust for solving unsteady Euler equations on fixed grid, their applicability, accuracy and robustness for solving compressible Euler equations in ALE formulation are relatively unexplored. The primary objective of this effort is to examine the performance, robustness, and accuracy of these schemes for solving unsteady compressible Euler equations on moving grid.

The most remarkable feature of the ALE formulation is that grid motion may be arbitrarily specified. This flexibility is often exploited to solve the moving boundary problems, such as wing flutter, periodic pitching of an airplane, and store separation from flight vehicles, where the grid velocity at the moving boundary is defined by the moving boundary motion. Alternatively, by appropriate definition of the grid

velocity, a Lagrangian surface can be established in the computational domain for the purpose of distinguishing and tracking material interface boundaries. By definition, a Lagrangian surface is established at a control surface by setting the interface velocity equal to the fluid velocity at the interface. This can be done as long as the fluid velocity is defined and continuous. After specifying the grid velocity at one point, for example, at a domain boundary or a contact surface, then it is usually a simple matter to construct a suitable distribution of grid velocity at all other points in the domain.

### 4.1. AUSM+ scheme on moving grids

The flux vector in ALE formulation can also be written as

$$\mathbf{F} = \begin{pmatrix} \mathbf{u} \cdot \mathbf{n}\rho \\ \mathbf{u} \cdot \mathbf{n}\rho\mathbf{v} + p\mathbf{n} \\ \mathbf{u} \cdot \mathbf{n}\rho H + p\dot{\mathbf{x}} \cdot \mathbf{n} \end{pmatrix}, \tag{4.5}$$

where $H = E + p/\rho$ is total enthalpy. The basic ideal behind Liou's AUSM+ [10] scheme is to recognize convection and acoustic waves as two distinct processes and consists in treating them separately

$$\mathbf{F} = \mathbf{F}^c + \mathbf{F}^p. \tag{4.6}$$

In the ALE formulation,

$$\mathbf{F}^c = Mr\,c\mathbf{\Phi}, \quad \mathbf{\Phi} = \begin{pmatrix} \rho \\ \rho\mathbf{v} \\ \rho H \end{pmatrix}, \quad \mathbf{F}^p = \begin{pmatrix} 0 \\ p\mathbf{n} \\ p\dot{\mathbf{x}} \cdot \mathbf{n} \end{pmatrix}, \tag{4.7}$$

where Much number relative to the interface velocity $Mr = (\mathbf{u} \cdot \mathbf{n})/c$ and the term $p\dot{\mathbf{x}} \cdot \mathbf{n}$ appears. In fact, this term can be splitted as a pure pressure term because $\dot{\mathbf{x}}$, i.e., the interface mesh velocity, has the same value on the left and on the right of the interface. The numerical flux of the AUSM+ at the interface $ij$, when generalized to accommodate an interface moving with velocity $\dot{\mathbf{x}}$, can be expressed as

$$\mathbf{F}_{ij}^{\text{AUSM+}} = \frac{1}{2}[Mr_{ij}c_{ij}(\mathbf{\Phi}_i + \mathbf{\Phi}_j) - c_{ij}|Mr_{ij}|(\mathbf{\Phi}_i - \mathbf{\Phi}_j)] + \begin{pmatrix} 0 \\ p\mathbf{n} \\ p\dot{\mathbf{x}} \cdot \mathbf{n} \end{pmatrix}_{ij}, \tag{4.8}$$

where the numerical speed of sound at the interface $c_{ij}$ is computed by the simple average formula

$$c_{ij} = \frac{1}{2}(c_i + c_j). \tag{4.9}$$

Let

$$Mr_i = \frac{\mathbf{u}_i \cdot \mathbf{n}}{c_{ij}}, \tag{4.10}$$

and

$$Mr_j = \frac{\mathbf{u}_j \cdot \mathbf{n}}{c_{ij}}. \tag{4.11}$$

The interface Mach number and pressure are then computed as a sum of two individual components, respectively,

$$Mr_{ij} = \mathcal{M}_{(4,\beta)}^+(Mr_i) + \mathcal{M}_{(4,\beta)}^-(Mr_j), \tag{4.12}$$

$$p_{ij} = \mathscr{P}^+_{(5,\alpha)}(Mr_i)p_i + \mathscr{P}^-_{(5,\alpha)}(Mr_j)p_j, \tag{4.13}$$

where the split Mach numbers are defined as

$$\mathscr{M}^\pm_{(1)}(M) = \tfrac{1}{2}(M \pm |M|), \tag{4.14}$$

$$\mathscr{M}^\pm_{(2)}(M) = \begin{cases} \mathscr{M}^\pm_{(1)}(M), & \text{if } |M| \geqslant 1; \\ \pm\tfrac{1}{4}(M \pm 1)^2, & \text{otherwise,} \end{cases} \tag{4.15}$$

$$\mathscr{M}^\pm_{(4,\beta)} = \begin{cases} \mathscr{M}^\pm_{(1)}(M), & \text{if } |M| \geqslant 1, \\ \mathscr{M}^\pm_{(2)}(M)[1 \mp 16\beta\mathscr{M}^\mp_{(2)}(M)], & \text{otherwise,} \end{cases} \tag{4.16}$$

$$\mathscr{P}^\pm_{(5,\alpha)}(M) = \begin{cases} \tfrac{1}{M}\mathscr{M}^\pm_{(1)}(M), & \text{if } |M| \geqslant 1; \\ \pm\mathscr{M}^\pm_{(2)}(M)[(2 \mp M) - 16\alpha M\mathscr{M}^\mp_{(2)}(M)], & \text{otherwise,} \end{cases} \tag{4.17}$$

with $\alpha = 3/16$, and $\beta = 1/8$.

This AUSM+ scheme has been used to compute the unsteady flows with moving boundaries and yields reasonably good results [18].

## 4.2. HLLC scheme on moving grids

The particular version of the HLLC flux [11] used in this work is defined by

$$\mathbf{F}^{\text{HLLC}}_{ij} = \begin{cases} \mathbf{F}_i, & \text{if } S_i > 0, \\ \mathbf{F}(\mathbf{U}^*_i), & \text{if } S_i \leqslant 0 < S_M, \\ \mathbf{F}(\mathbf{U}^*_j), & \text{if } S_M \leqslant 0 \leqslant S_j, \\ \mathbf{F}_j, & \text{if } S_j < 0, \end{cases} \tag{4.18}$$

where

$$\mathbf{U}^*_i = \begin{pmatrix} \rho^*_i \\ (\rho\mathbf{v})^*_i \\ (\rho E)^*_i \end{pmatrix} = \frac{1}{S_i - S_M} \begin{pmatrix} (S_i - u_{n_i})\rho_i \\ (S_i - u_{n_i})(\rho\mathbf{v})_i + (p^* - p_i)\mathbf{n} \\ (S_i - u_{n_i})(\rho E)_i - p_i u_{n_i} + p^* S_M \end{pmatrix}, \tag{4.19}$$

$$\mathbf{U}^*_j = \begin{pmatrix} \rho^*_j \\ (\rho\mathbf{v})^*_j \\ (\rho E)^*_j \end{pmatrix} = \frac{1}{S_j - S_M} \begin{pmatrix} (S_j - u_{n_j})\rho_j \\ (S_j - u_{n_j})(\rho\mathbf{v})_j + (p^* - p_j)\mathbf{n} \\ (S_j - u_{n_j})(\rho E)_j - p_j u_{n_j} + p^* S_M \end{pmatrix}, \tag{4.20}$$

$$\mathbf{F}^*_i \equiv \mathbf{F}(\mathbf{U}^*_i) = \begin{pmatrix} S_M\rho^*_i \\ S_M(\rho\mathbf{v})^*_i + p^*\mathbf{n} \\ S_M(\rho E)^*_i + (S_m + \dot{\mathbf{x}} \cdot \mathbf{n})p^* \end{pmatrix}, \tag{4.21}$$

$$\mathbf{F}^*_j \equiv \mathbf{F}(\mathbf{U}^*_j) = \begin{pmatrix} S_M\rho^*_j \\ S_M(\rho\mathbf{v})^*_j + p^*\mathbf{n} \\ S_M(\rho E)^*_j + (S_m + \dot{\mathbf{x}} \cdot \mathbf{n})p^* \end{pmatrix}, \tag{4.22}$$

$$p^* = \rho_i(u_{n_i} - S_i)(u_{n_i} - S_M) + p_i = \rho_j(u_{n_j} - S_j)(u_{n_j} - S_M) + p_j, \tag{4.23}$$

and $u_n = \mathbf{u} \cdot \mathbf{n}$. $S_M$ is defined as

$$S_M = \frac{\rho_j u_{n_j}(S_j - u_{n_j}) - \rho_i u_{n_i}(S_i - u_{n_i}) + p_i - p_j}{\rho_j(S_j - u_{n_j}) - \rho_i(S_i - u_{n_i})}. \tag{4.24}$$

Signal velocities $S_i$, and $S_j$ are defined as

$$S_i = \min[u_{n_i} - c_i, (\hat{\mathbf{v}} - \dot{\mathbf{x}}) \cdot \mathbf{n} - \hat{c}], \tag{4.25}$$

$$S_j = \max[u_{n_j} + c_j, (\hat{\mathbf{v}} - \dot{\mathbf{x}}) \cdot \mathbf{n} + \hat{c}], \tag{4.26}$$

with $\hat{\mathbf{v}}$ and $\hat{c}$ being Roe's average variables for velocity and speed of sound.

This HLLC flux is found to have the following properties: (1) exact preservation of isolated contact and shear waves, (2) positivity-preserving of scalar quantity, (3) enforcement of entropy condition.

### 4.3. Approximate Godunov scheme on moving grids

The approximate Riemann problem solver for a general EOS, developed by Colella [12], starts with the calculation of $(p^*, u_n^*)$ by $q$:

$$p^* = \frac{W_j p_i + W_i p_j + W_i W_j(u_{n_i} - u_{n_j})}{W_i + W_j}, \tag{4.27}$$

$$u_n^* = \frac{W_i u_{n_i} + W_j u_{n_j} + p_i - p_j}{W_i + W_j}, \tag{4.28}$$

where $W = \rho c$. The remainder of the $*$-state calculation proceeds as follows:

$$\rho_{i,j}^* = \rho_{i,j} + \frac{p^* - p_{i,j}}{c_{i,j}^2}, \tag{4.29}$$

$$(c_{i,j}^*)^2 = \frac{p^* \rho_{i,j} c_{i,j}^2}{p_{i,j} \rho_{i,j}^*}, \tag{4.30}$$

$$(\rho e)_{i,j}^* = (\rho e)_{i,j} + (p^* - p_{i,j})\left(\frac{e + p/\rho}{c^2}\right)_{i,j}, \tag{4.31}$$

$$u_{t_{i,j}}^* = u_{t_{i,j}}, \tag{4.32}$$

where $u_t = \mathbf{u} \cdot \mathbf{t}$ is the tangential velocity with $\mathbf{t}$ being the unit tangential vector. The (approximate) Godunov state $\mathbf{Q}_G$ is defined to be the value of $\mathbf{Q} = (\rho, \mathbf{u}, \rho e, p)^t$ along the ray $x/t = 0$ and is computed in two steps. First, we set

$$\mathbf{Q}, \mathbf{Q}^* = \begin{cases} \mathbf{Q}_i, \mathbf{Q}_i^* & \text{if } u_n^* > 0, \\ \mathbf{Q}_j, \mathbf{Q}_j^* & \text{otherwise,} \end{cases} \tag{4.33}$$

and

$$\lambda, \lambda^* = c - su_n, c^* - su_n^*, \tag{4.34}$$

where $s = \text{sign}(u_n^*)$. Also, an approximate shock speed

$$\sigma = \frac{1}{2}(\lambda + \lambda^*) \tag{4.35}$$

is computed. Second, if $\lambda^* > \lambda$, then

$$\mathbf{Q}_G = \begin{cases} \mathbf{Q} & \text{if } \sigma < 0, \\ \mathbf{Q}^* & \text{otherwise,} \end{cases} \tag{4.36}$$

otherwise, if $\lambda^* < \lambda$, then

$$\mathbf{Q}_G = \begin{cases} \mathbf{Q} & \text{if } \lambda < 0, \\ \mathbf{Q}^* & \text{if } \lambda^* > 0, \\ \alpha\mathbf{Q}^* + (1 - \alpha)\mathbf{Q} & \text{otherwise.} \end{cases} \tag{4.37}$$

Here, $\alpha = \frac{1}{2}(1 + \frac{\lambda + \lambda^*}{\lambda - \lambda^*})$. These two steps guarantee entropy-satisfying waves; the last equation implements linear interpolation in the wave speed to approximate the solution inside a rarefaction fan. The conservative flow variable vector at the interface can then be computed from the Godunov variable vector as

$$\mathbf{U}_{ij} = \begin{pmatrix} \rho_{ij} \\ (\rho\mathbf{v})_{ij} \\ (\rho E)_{ij} \end{pmatrix} = \begin{pmatrix} \rho_G \\ \rho_G(\mathbf{u}_G + \dot{\mathbf{x}}) \\ (\rho e)_G + 0.5\rho_G|\mathbf{u}_G + \dot{\mathbf{x}}|^2 \end{pmatrix}. \tag{4.38}$$

Finally, the fluxes for flow equations at the interface can be evaluated from the Godunov state as follows:

$$\mathbf{F}_{ij} = \begin{pmatrix} \mathbf{u}_G\rho_{ij} \\ \mathbf{u}_G(\rho\mathbf{v})_{ij} + p_G\mathbf{n} \\ \mathbf{u}_G((\rho E)_{ij} + p_G) + p_G\dot{\mathbf{x}} \cdot \mathbf{n} \end{pmatrix}. \tag{4.39}$$

It is worth noting: (1) The description of these three schemes does not assume any particular form of EOS. Hence, they can be used to compute real fluids with a general EOS, as long as the interrogation of the state relations for pressure and speed of sound is known; (2) At the Lagrangian contact where $p_i = p_j$, $\mathbf{u} = 0$, the dissipation vanishes for all three schemes. This fact easily explains why the contact discontinuities can be sharply resolved by the moving grid methods; (3) In the absence of grid motion, all three schemes are shown to recover exactly their Eulerian formulation; and (4) In the case of uniform free stream flow conditions, all three schemes lead to the GCL. This fact might seem trivial, but is extremely important to ensure that no error is introduced due to the ALE formulation, as the implementation of these schemes can easily violate this property.

## 5. Numerical examples

All computations used an explicit four-stage Runge–Kutta time-stepping scheme to advance the solution in time, and a CFL number of 0.85. The second order accuracy in space is achieved using reconstruction algorithm based on the primitive variables and MUSCL approach [19]. The Van Albada limiter [27] is employed to eliminate spurious oscillations in the vicinity of discontinuities. The first four test cases are chosen to validate the numerical schemes and assess the solution accuracy, where the following Tammann EOS [5] is used in the computation

$$p = (\gamma - 1)\left(\rho e - \frac{\rho \mathbf{V}^2}{2} - P_c\right) - P_c,$$

and the speed of sound is computed according to

$$C^2 = \gamma \frac{p + P_c}{\rho},$$

where $\gamma$ is the ratio of specific heats and $P_c$ is a prescribed pressure-like constant. These values can be assigned to describe the material property of interests, such as stiffened polytropic gas. The computational results for these cases were obtained on a grid of 101 points. A Lagrangian surface is established at the contact discontinuity, and the grid velocity is tapered linearly to zero at both ends of the computational domain.

### 5.1. Material interface problem

The first test case is the material interface problem, whose solution represents a single contact discontinuity in gas dynamics. A shocktube is filled with low-density fluid on the left and high-density on the right under different ratios of specific heat. Velocity and pressure equilibrium are assumed along the whole tube. The initial conditions in the present computation are the following:

$$\rho = 1.000, \quad u = 1, \quad p = 1, \quad \gamma = 1.4, \quad P_c = 0, \quad 0 \leqslant x < 50,$$

$$\rho = 0.125, \quad u = 1, \quad p = 1, \quad \gamma = 1.2, \quad P_c = 0, \quad 50 \leqslant x \leqslant 100,$$

where the solution of this Riemann problem consists of a single contact discontinuity in gas dynamics. The solutions obtained by the three schemes AUSM+, HLLC, and approximate Godunov at time $t = 20$ are presented in Fig. 1. The three schemes are all able to capture the exact solution, demonstrating the ability of the ALE formulation to sharply capture the Lagrangian contact discontinuity. The criterion of free-stream conserving is clearly satisfied by all three schemes, which has proved invaluable to validate the implementation of ALE formulation.

### 5.2. Single material Sod shocktube problem

The well-known Sod shocktube problem is considered in this test case, whose solution contains simultaneously a shock wave, a contact discontinuity, and an expansion fan. The initial conditions in the present computation are the following:

$$\rho = 1.000, \quad u = 0, \quad p = 1.0, \quad \gamma = 1.4, \quad P_c = 0, \quad 0 \leqslant x < 50,$$

$$\rho = 0.125, \quad u = 0, \quad p = 0.1, \quad \gamma = 1.4, \quad P_c = 0, \quad 50 \leqslant x \leqslant 100.$$

This test case was chosen to test and assess the accuracy of the ALE solution by comparing with the Eulerian solution, as the problem can be solved using either the Eulerian or the ALE formulation. Fig. 2(a) and (b) compare the first order and second order ALE solutions with the Eulerian solutions at $t = 20$ obtained by AUSM+, HLLC, and Godunov schemes, respectively. As expected, the first order solutions obtained by all three schemes are monotonic on the fixed grid. Both the HLLC and Godunov schemes are also able to produce monotonic solutions on the moving grid. However, the ALE AUSM+ scheme fails to yield the monotonic solution, as small oscillations near the material interface are clearly visible. Both fixed and moving grid results are in good agreement with the exact solution for this case, although the ALE
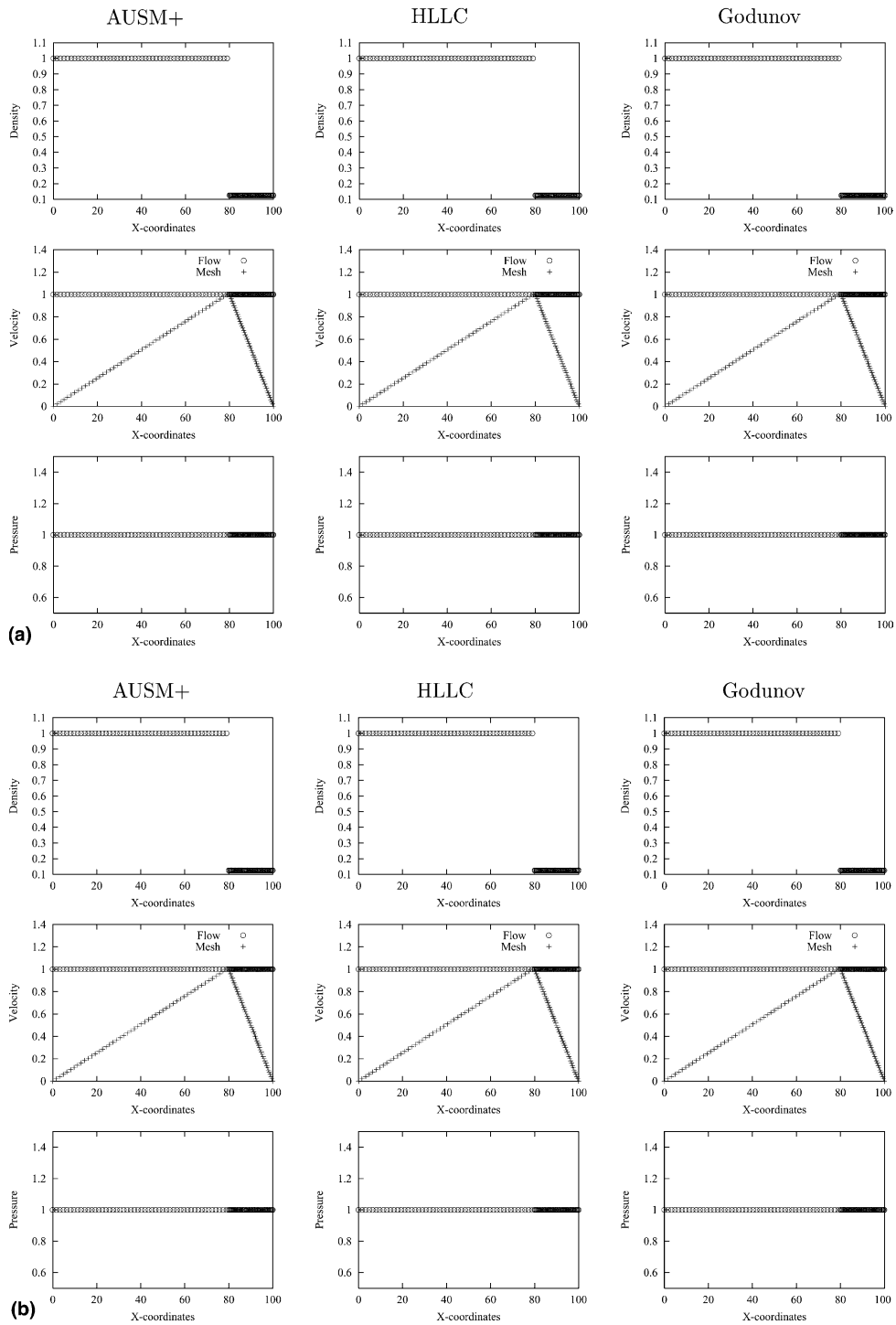
Fig. 1. Computed first order (a) and second order (b) solutions for the multi-component interface problem at $t = 20$ by AUSM+, HLLC, and Godunov schemes using ALE formulation on 101 grid points.
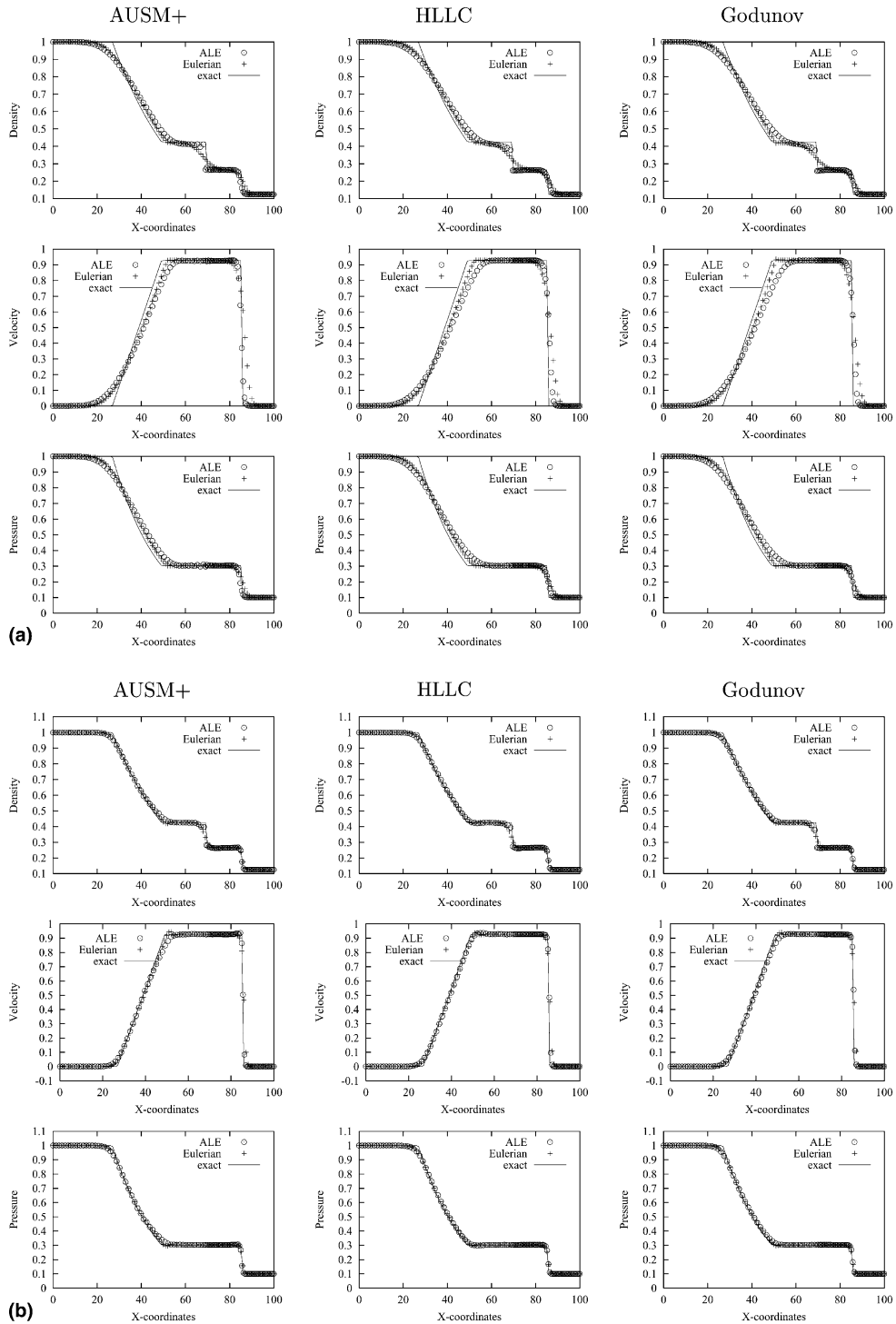
Fig. 2. Comparison of first order (a) and second order (b) Eulerian and ALE solutions for the Sod shocktube problem at $t = 20$ obtained by AUSM+, HLLC, and Godunov schemes on 101 grid points.

solution is found to be less dissipative than its Eulerian counterpart, and gives better resolution at maintaining sharp contact discontinuity.

### 5.3. Shocktube problem with different Gamma

The Sod shocktube problem, now with two different ideal gases, is considered in this test case. The initial conditions in the present computation are the following:

$$\rho = 1.000, \quad u = 0, \quad p = 1.0, \quad \gamma = 1.667, \quad P_c = 0, \quad 0 \leqslant x < 50,$$

$$\rho = 0.125, \quad u = 0, \quad p = 0.1, \quad \gamma = 1.200, \quad P_c = 0, \quad 50 \leqslant x \leqslant 100.$$

Figs. 3(a) and (b) show the first order and second order ALE solutions at $t = 20$ obtained by the AUSM+, HLLC, and Godunov schemes, respectively. Although profiles from the first order solutions obtained by the HLLC and Godunov schemes are fairly smeared, a typical result for first order solutions, clean and monotonic solutions are obtained. However, the AUSM+ scheme is unable to produce a monotonic solution, generating small oscillations around the contact discontinuity. It is worth noting that the material interface is sharply captured in both the first and second order solutions and computations with a second order scheme tend to improve solutions significantly for both the shock wave and the rarefraction wave. Note though that a small amount of numerical diffusion at the material interface does exist. This diffusion can be attributed to the first order scheme used in the material interface. However, this should not be viewed as a setback for the present approach, as a second order scheme can easily lead to oscillation across the material interface, and a little oscillation can lead to collapse or meaningless of the computation for stiff EOS.

### 5.4. Gas/water shocktube problem

A two phase gas–liquid Riemann problem is considered here. The initial conditions in the present computation are the following:

$$\rho = 1.271000, \quad u = 0, \quad p = 9.119252E + 09, \quad \gamma = 1.4, \quad P_c = 0, \quad 0 \leqslant x < 50,$$

$$\rho = 0.999983, \quad u = 0, \quad p = 1.013250E + 06, \quad \gamma = 7.0, \quad P_c = 3.03975E + 09, \quad 50 \leqslant x \leqslant 100.$$

This is an extremely difficult problem, since the equations of state for water and air are drastically different. Figs. 4(a) and (b) show the first order and second order ALE solutions at $t = 1.55921E - 04$, obtained by the AUSM+, HLLC, and Godunov schemes, respectively. The computed results for this difficult problem clearly indicate the deficiencies of the ALE AUSM+ scheme, giving rise to serious oscillations near both material interface and shock wave. However, both the first order ALE HLLC and Godunov schemes are able to yield monotonic, oscillation-free, and sharp contact solution. Computations with the second order schemes improve solutions significantly for both shock and rarefraction waves. This example clearly demonstrates the potential and robustness of the ALE HLLC and Godunov schemes for solving multi-material flows with strong shock wave and contact discontinuity.

### 5.5. Spherically symmetric underwater explosion

As an example of application, the developed three schemes were used to compute a benchmark 1D spherically symmetric underwater explosion problem. This represents a serious challenge to any multi-material computation methods, as the materials are drastically different, and the EOS for water is very stiff.
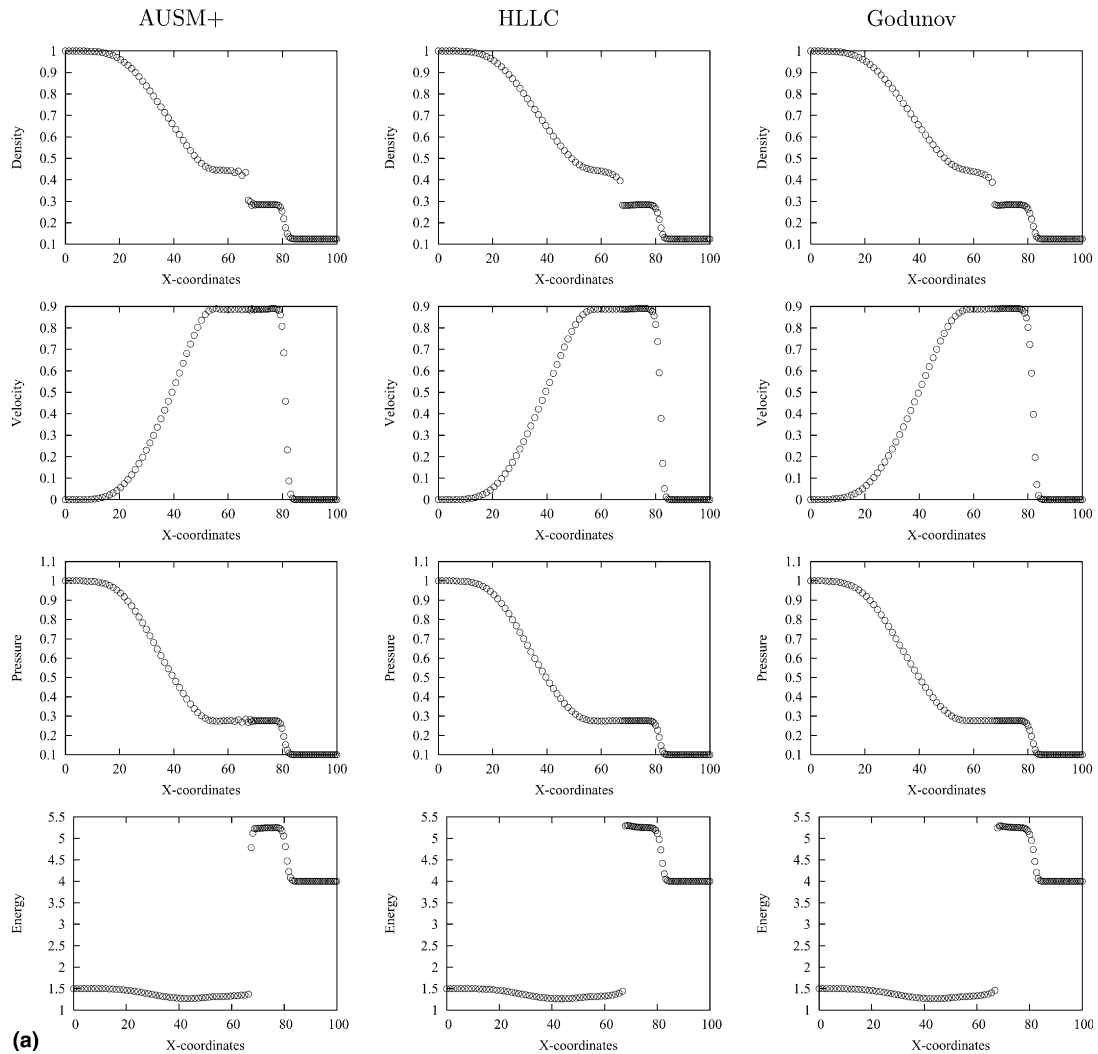
Fig. 3. (a) Computed first order solutions for the multi-component gas shocktube problem at $t = 20$ by AUSM+, HLLC, and Godunov schemes using ALE formulation on 101 grid points. (b) Computed second order solutions for the multi-component gas shocktube problem at $t = 20$ by AUSM+, HLLC, and Godunov schemes using ALE formulation on 101 grid points.

Any oscillations in the material interface will lead to invalid EOS (negative pressure), resulting in either collapse or meaningless of calculation. This difficult problem is chosen to test the ability of the described numerical methods to model multi-component problems with strong shocks and contact discontinuities. In addition, it is easy to assess the accuracy of the numerical solution, as the experimental data [20] is available and the problem has been investigated previously by several authors and a benchmark numerical solution exists [2]. The computational conditions are: detonation of 300 g of TNT spherical charge (radius of 3.5287 cm) at a depth of 91.4 m (ambient pressure of $1.0E + 07$ d/cm$^2$). The problem can be essentially regarded as a spherical two-phase shocktube problem where the initial conditions in cgs units are given by

$$\rho = 1.63000000, \;\; u = 0, \;\; e = 4.29E + 10, \quad 0.0 \leqslant x \leqslant 3.5287,$$
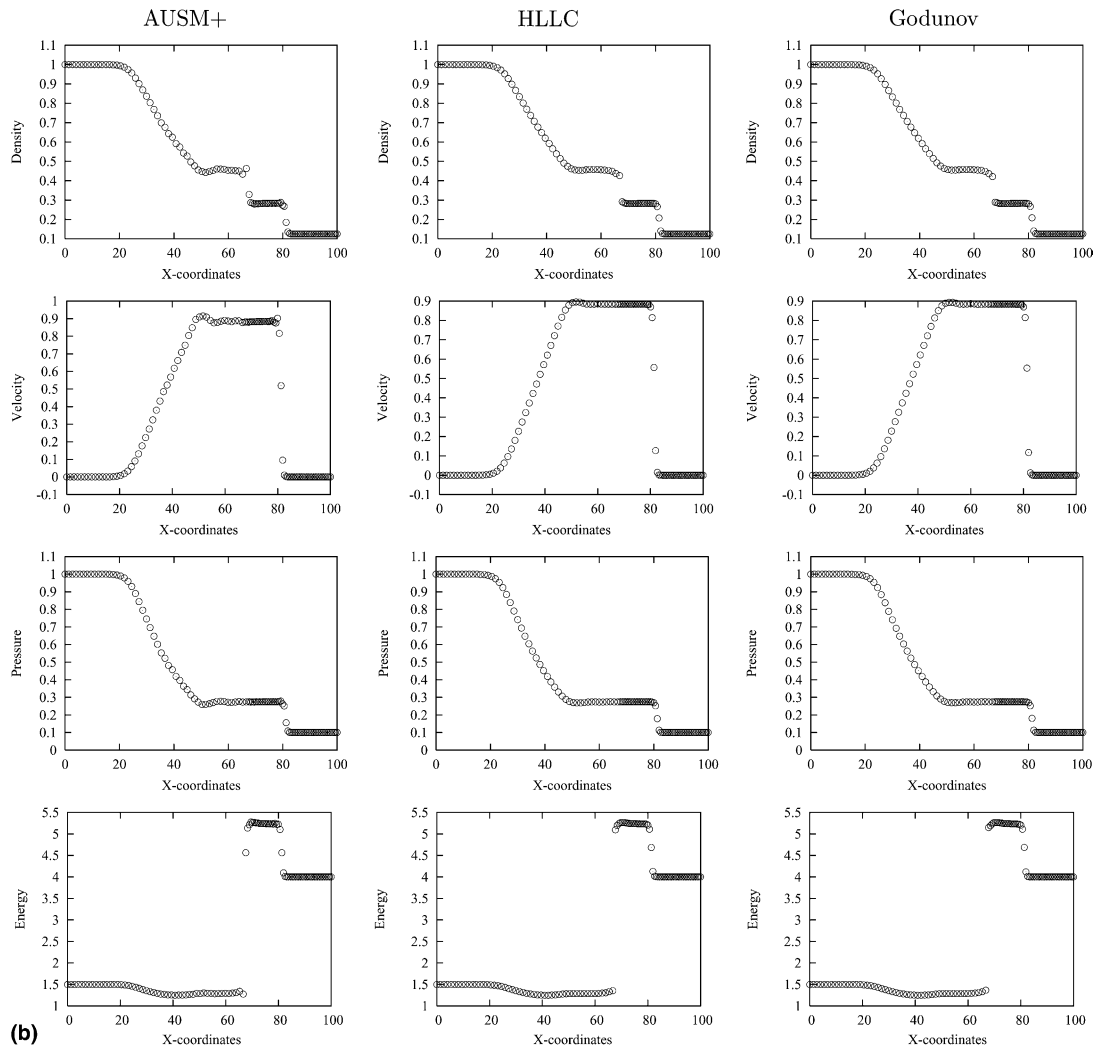
AUSM+ · · · HLLC · · · Godunov



Fig. 3 (*continued*)

$$\rho = 1.00037984, \quad u = 0, \quad p = 1.00\mathrm{E}+07, \quad 3.5287 < x \leqslant 25.$$

The Jones–Wilkins–Lee (JWL) and Tait equations of state are used for the detonation-products gas and liquid water, respectively:

$$\text{Tait}: \quad p = B\left[\left(\frac{\rho}{\rho_0}\right)^{\gamma} - 1\right] + A,$$

where

$$B = 3.31\mathrm{E}+09, \quad \rho_0 = 1.0,$$
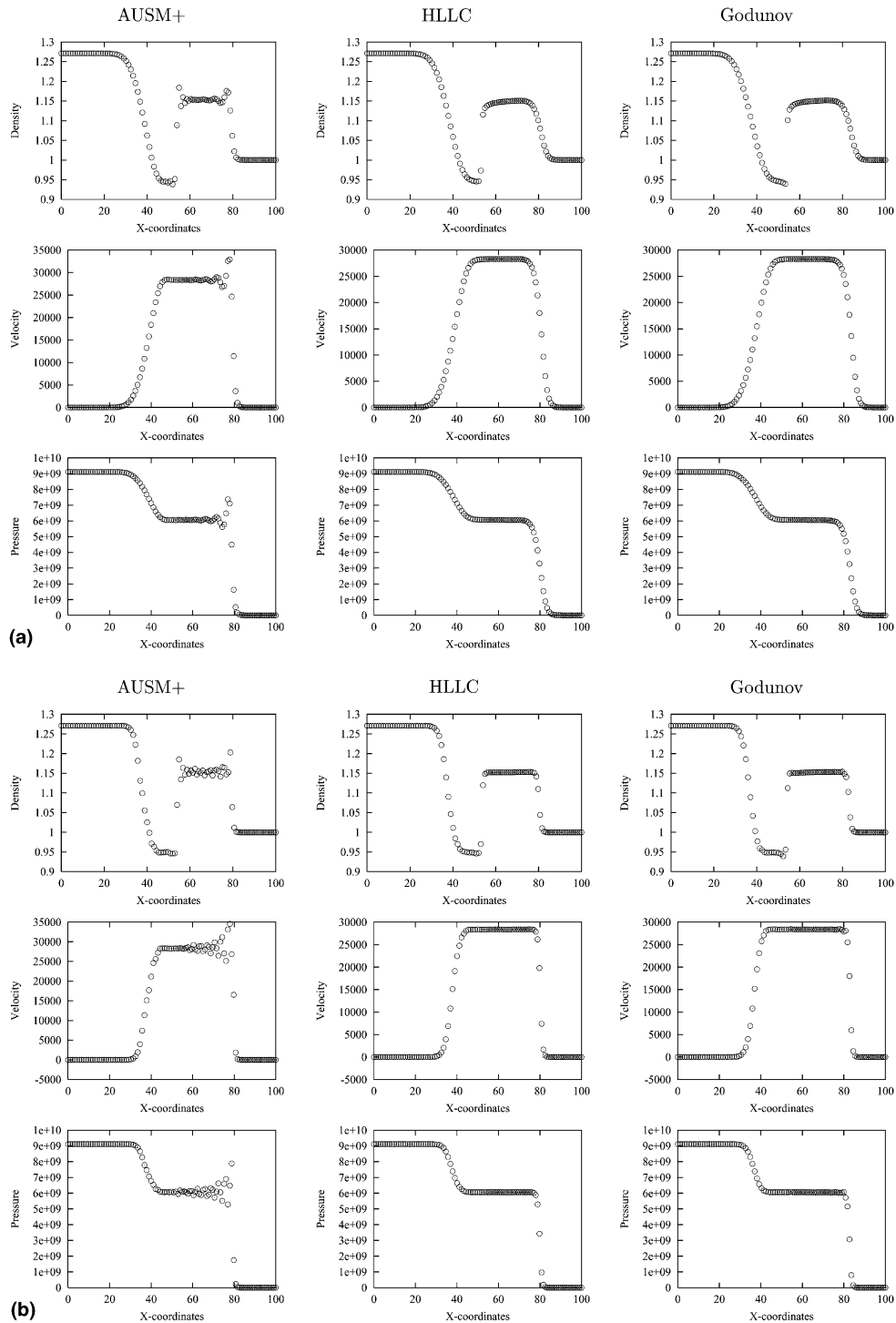
$$A = 1.0\mathrm{E}+06, \quad \gamma = 7.15.$$

Fig. 4. Computed first order (a) and second order (b) solutions for the multi-component gas/water shocktube problem at $t = 1.55921E - 04$ by AUSM+, HLLC, and Godunov schemes using ALE formulation on 101 grid points.

$$\text{JWL}: \quad p = A\left(1 - \frac{\omega\rho}{R_1\rho_0}\right)e^{-\frac{R_1\rho_0}{\rho}} + B\left(1 - \frac{\omega\rho}{R_2\rho_0}\right)e^{-\frac{R_2\rho_0}{\rho}} + \omega\rho e,$$

where

$$A = 7.712\text{E} + 12,$$

$$B = 0.0323\text{E} + 12,$$

$$R_1 = 4.15, \quad R_2 = 0.95, \quad \omega = 0.3,$$

$$\rho_0 = 1.63, \quad e_0 = 0.0429\text{E} + 12.$$

Note the speed of sound for Tait EOS is computed as

$$c^2 = \gamma\frac{p + A}{\rho}.$$

The computation was performed on a series of four grids in order to get a mesh converged solution. These grids contain 751, 1501, 3001, and 6001 uniform placed points, respectively. It is found that the mesh, that features 3001 points with 424 points in the bubble and 2577 grid points in the water, is adequate to provide a grid converged solution. A Lagrangian interface is established at the material interface by constraining the grid velocity to match the fluid velocity at the interface. The grid velocity is further constrained by setting it to be zero at the origin and $V_{max} + C_{max}$ at the outer boundary of the domain, where the $V_{max}$ and $C_{max}$ are the maximal velocity and speed of sound for water, respectively. At intermediate points between these constraints the grid velocity is linearly interpolated. The computation was performed using the three HLLC, Godunov, and AUSM+ schemes, respectively. It is found that both HLLC and Godunov methods produced the virtually identical results, however the ALE AUSM+ scheme generated erroneous oscillations around the gas/water interface, which ultimately lead to the collapse of the computation. Unless stated otherwise, the numerical results to be presented here are obtained using ALE Godunov scheme on the 3001 grid-points mesh.

Figs. 5(a)–(d) show the evolution of the computed solution through different phases of spherically symmetric underwater explosion problem. The initial phase, illustrated in Fig. 5(a) starts with a primary shock wave traveling to the right into the water and an expansion wave moving to the left toward the bubble origin. The expansion wave reflects from the origin as an expansion, resulting in a region of very low pressure near the origin. The outward inertia of the expanding gas is eventually overcome by the centripetal pressure gradient and the gas reverses direction, forming an inward moving shock wave which in turn reflects as a shock wave from the origin. This reflected secondary shock wave then propagates outward toward the gas/water interface. Note the shock wave is accurately resolved and material interface is sharply captured without any oscillations due to the ALE formulation.

Fig. 5(b) shows the shock and free-surface interaction phase, where the secondary shock wave propagates to the gas/water interface and interacts with it. This interaction generates a reflected shock wave which moves back into the bubble toward the origin, and a transmitted shock wave that travels outward from the bubble into the water. This process repeats numerous times, each time at a reduced shock strength, as shown in Fig. 5(c) where the primary, secondary, and tertiary shock waves are clearly visible in the pressure time history plot.

The evolution of the pressure and density profiles through bubble collapse phase is illustrated in Fig. 5(d) where one can clearly see that at the bubble minimum volume, a compression pressure pulse, called bubble impulse, is emitted from the bubble.
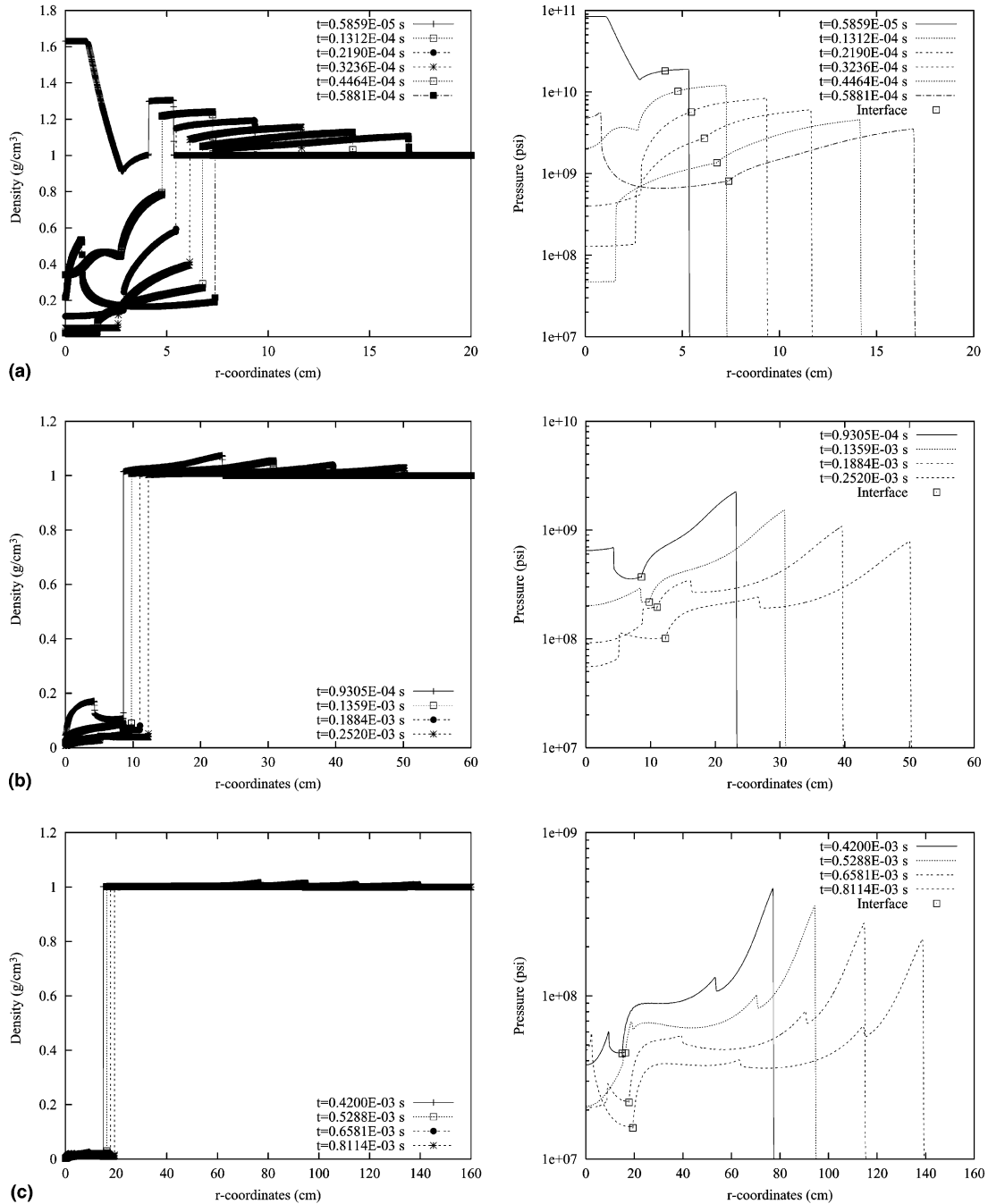
Fig. 5. (a) Density and pressure distributions during the initial phase of spherically symmetric underwater explosion problem. (b) Density and pressure distributions during the shock/material–surface interaction phase of spherically symmetric underwater explosion problem. (c) Density and pressure distributions during the incompressible phase of spherically symmetric underwater explosion problem. (d) Density and pressure distributions during the bubble collapse phase of spherically symmetric underwater explosion problem. (e) Comparison of bubble radius time and interface pressure history for different mesh size solutions of the spherically symmetric underwater explosion problem.

**(d)**



**(e)**
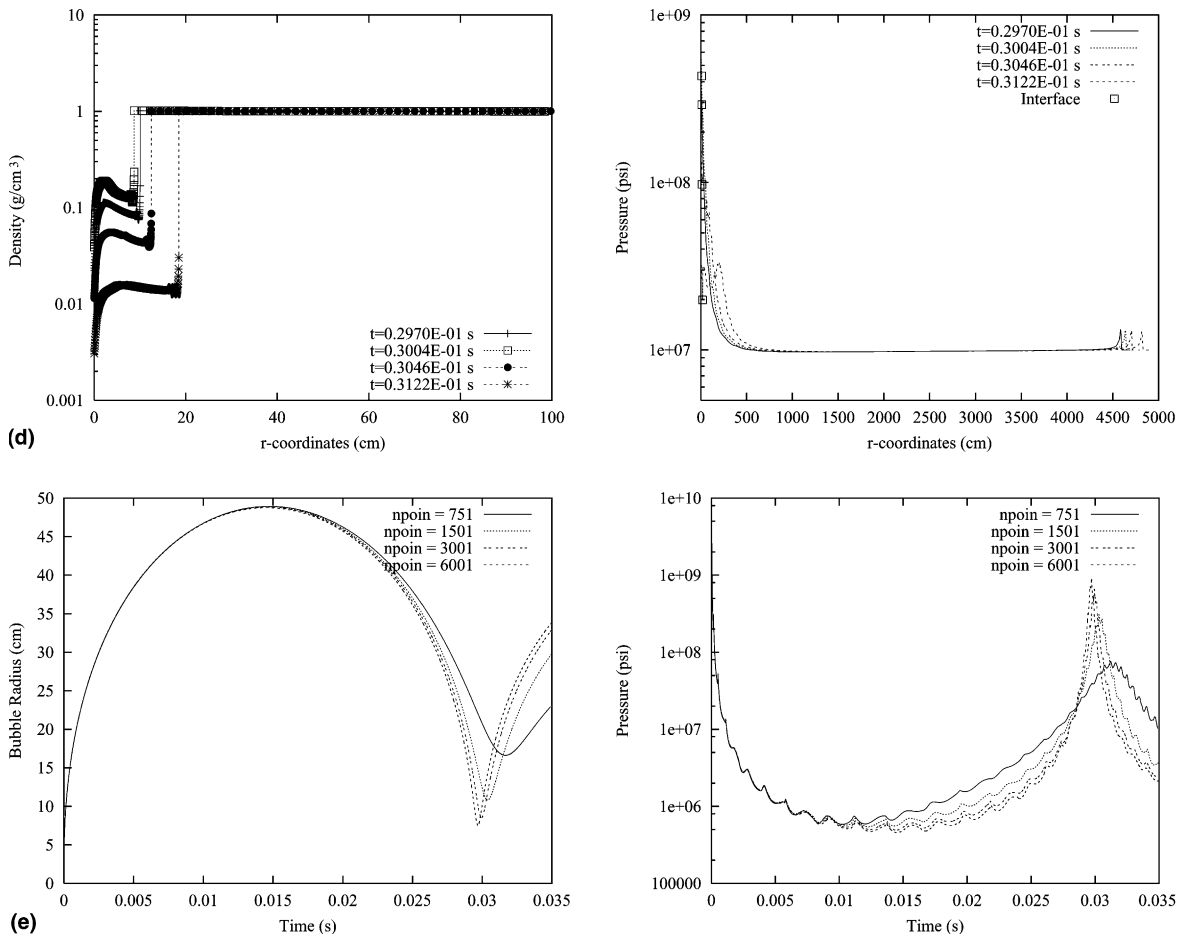
Fig. 5. (*continued*)

As mentioned before, a grid convergence study has been performed on a series of four grids to provide insight and guideline into grid resolution requirements for underwater explosion bubble problem. The bubble radius and the bubble–water interface pressure time history for all four grids are compared in Fig. 5(e). The oscillations of interface pressure are clearly present due to the interactions of the shock waves inside the bubble with the gas/water interface. This type of oscillatory interface behavior has been previously observed by Mader [21], and later confirmed by Wardlaw et al. [2]. The grid density has significant impact on the bubble period, however the maximum bubble radius differs very little among those four grids. Table 1 shows a detailed comparison among the four grids and the experimental data of Swift and Decius [20]. The difference of the solutions between the last two grids is insignificant, indicating a converged solution can be considered as a grid converged solution on the third grid, which has 3001 grid points with 424 grid points in the bubble. From these results, it can be seen that the present computation has clearly captured all of the important physical phenomena: initial primary shock wave, shock wave and material–surface interaction, and the pressure pulses from bubble collapse and rebound. The computed bubble period and maximum radius are in good agreement with experimental data, clearly demonstrating the accuracy of the purposed numerical methods. Note that the maximum radius is converging to a larger value

than observed experimentally. This is mainly due to the fact that the same uniform TNT conditions are used as the initial bubble state. Dr. Wardlaw et al. [2] shown that they got the same maximum radius as experimental one, if they use the so-called non-uniform Euler model, where the distribution of properties within the bubble is determined using a spherical analog to the Taylor plane wave solution based on the work of Guirguis. The resulting bubble property profile features the highest pressure at the bubble/water interface with a constant minimum pressure region at the bubble center.

### 5.6. Supersonic missile over water

This test case is designed to investigate the behavior of the refraction of a bow wave generated by a supersonic missile flying above the ocean. The computation shows a missile with the shape of an ellipse of diameters 3 by 0.5 m, traveling at 500 meters per second at an altitude of 5 m above a flat body of water. The initial conditions in cgs units in the computation are the following:

$$\rho = 0.001225, \quad u = 50000, \quad v = 0, \quad p = 1013250, \quad \gamma = 1.4, \quad P_c = 0 \quad \text{for air},$$

$$\rho = 1, \quad u = 50000, \quad v = 0, \quad p = 1013250, \quad \gamma = 7, \quad P_c = 3.03975\text{E} + 09 \quad \text{for water}.$$

Note that the perfect gas EOS is used for air and Tammann EOS is used for water. The computational mesh containing 37,373 points and 74,067 elements is shown in Fig. 6(a). The computed pressure contours obtained using HLLC method and displayed in Fig. 6(b) show good resolution of both reflected shock wave and refraction wave at the water/air interface. This example clearly demonstrates that the ALE formulation is especially attractive for problems where the material interface does not submit big deformation and the resolution of contact surfaces is important. Fig. 6(c) shows the shape of water/air interface, where the small interface deformation is very well resolved. Clearly any capturing methods will have the difficulty to capture such small deformation. Note that pure Lagrangian method will fail for this problem, as the flow experiences a significant shear across the material interface, which can clearly be seen in Fig. 6(d) where the velocity distribution for both air and water along the material interface is shown.

### 5.7. 2D underwater explosion

In this example, a 2D underwater explosion inside a water tank is computed using ALE HLLC method. The test case is designed to investigate the early stage of underwater explosion problems, namely the propagation of primary shock waves and the dynamics of shock–bubble interaction. The problem can be essentially regarded as a two dimensional two-material flow problems, where the initial conditions in cgs units are given by

$$\rho = 1.00037984, \quad u = 0, \quad p = 1.00\text{E} + 07, \quad 0 \leqslant x \leqslant 15, \quad -8 \leqslant y \leqslant 15, \quad r > 3.5287,$$

$$\rho = 1.63000000, \quad u = 0, \quad e = 4.29\text{E} + 10, \quad 0.0 \leqslant r \leqslant 3.5287,$$

Table 1
Computation and experiment for underwater explosion bubble (grid convergence study)

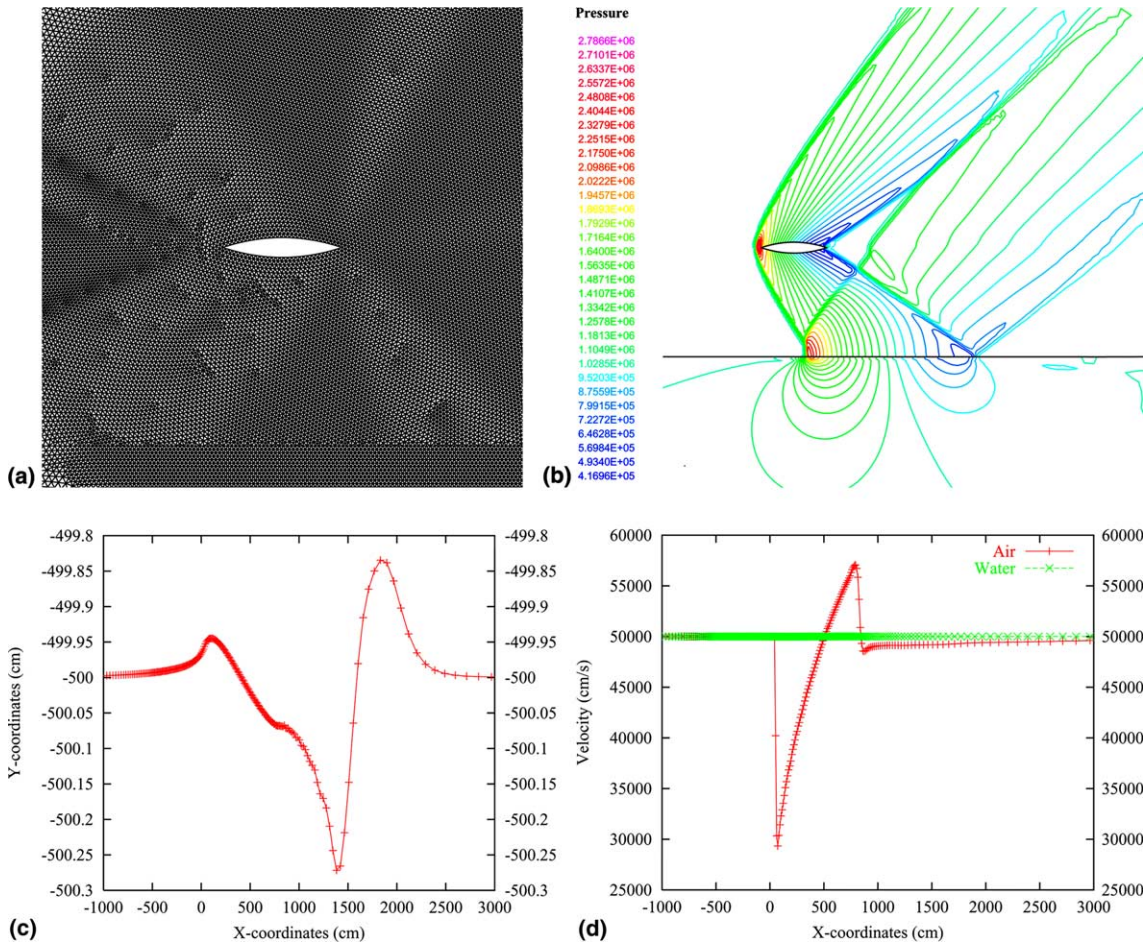| Grid size | Period (ms) | Error (%) | $R_{max}$ (cm) | Relative error (%) |
|---|---|---|---|---|
| 751 (106) | 31.65596 | 6.2 | 48.92498 | 5.45 |
| 1501 (212) | 30.39513 | 2.0 | 48.88203 | 5.35 |
| 3001 (424) | 29.94145 | 0.47 | 48.83771 | 5.25 |
| 6001 (847) | 29.70043 | −0.33 | 48.75348 | 5.07 |
| Experiment | 29.8 | 0 | 46.4 | 0 |

Fig. 6. (a) Mesh used for computing a missile flying above the ocean. (nelem = 74,067, npoin = 37.373). (b) Computed pressure contours for a flying missile above the ocean at a speed of 50,000 cm/s. (c) The water/air material interface shape for flying missile simulation. (d) Computed velocity distribution of water and air along the water/air material interface.

where $r = \sqrt{x^2 + y^2}$. The same JWL and Tait equations of state for test problem E are used for the detonation-products gas and water, respectively. The initial and final meshes in the vicinity of the bubble used in the computation, shown in Fig. 7(g) contain 60,121 points, 119,286 elements, and 138 material interface points, where one can see that an uniform mesh at the beginning of the computation becomes severely distorted in the water region as a result of the bubble expansion. Fig. 7(h) shows the $X$- and $Y$-components of grid velocity, which are obtained by solving a Laplace equation. The bubble shapes at different times are displayed in Fig. 7(i), where the interaction between bubble and the reflected shock wave causes the unsymmetrical bubble. Figs. 7(a)–(f) shows the evolution of the computed density, velocity, and pressure contours at different times. The simulation starts with a primary shock wave traveling into the water and an expansion wave moving in the bubble toward the bubble origin (Fig. 7(a)). The primary shock wave then hits the bottom of the tank and the resulting reflected shock wave is then moving toward the water/gas bubble interface (Fig. 7(b)). After the interaction with the bubble, this reflected shock wave is diffracted into two waves (Fig. 7(c)): a reflected rarefraction wave moving into the water and a transmitted shock wave in
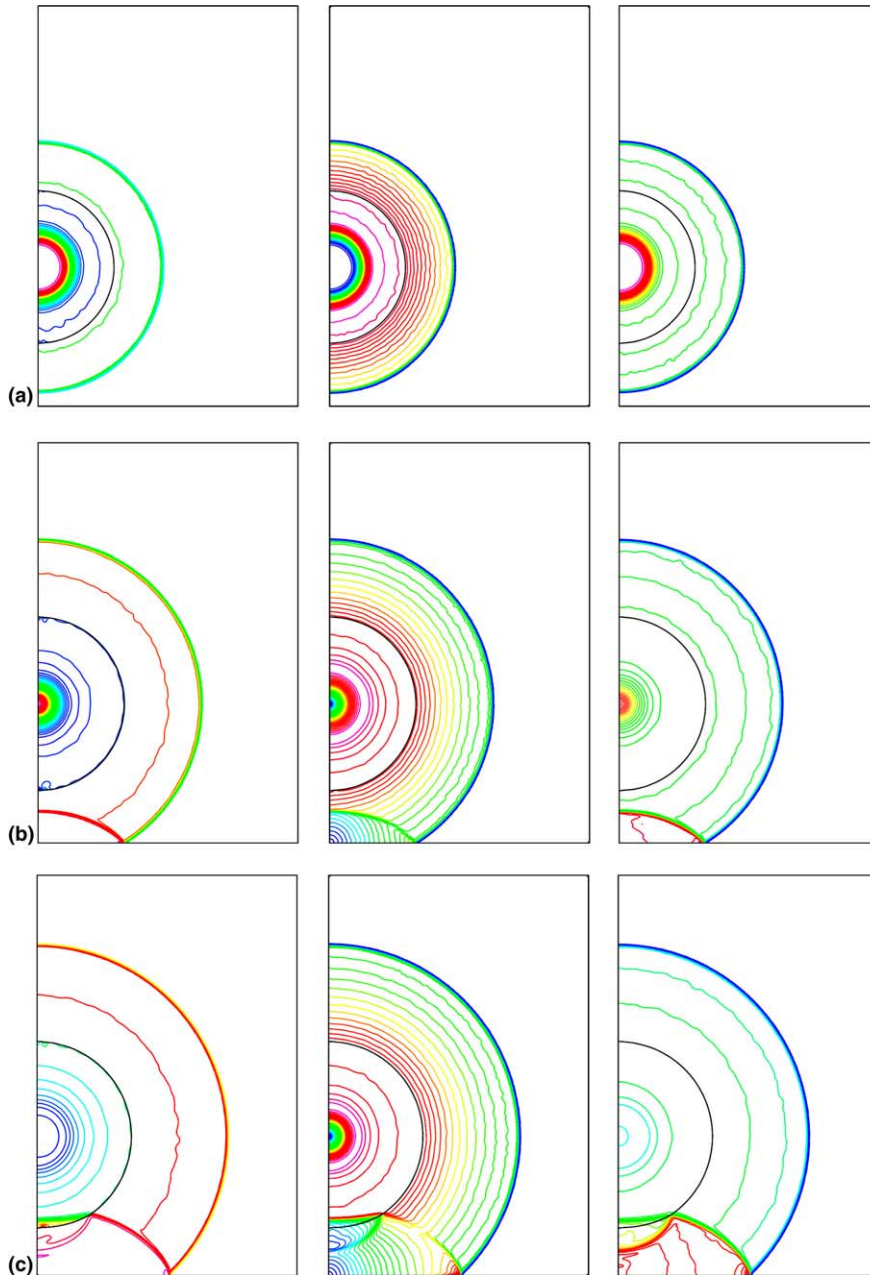
Fig. 7. (a) Computed density, velocity, pressure contours at $t = 0.1542E − 04$ s for 2D underwater explosion problem. (b) Computed density, velocity, pressure contours at $t = 0.2523E − 04$ s for 2D underwater explosion problem. (c) Computed density, velocity, pressure contours at $t = 0.3249E − 04$ s for 2D underwater explosion problem. (d) Computed density, velocity, pressure contours at $t = 0.4015E − 04$ s for 2D underwater explosion problem. (e) Computed density, velocity, pressure contours at $t = 0.4893E − 04$ s for 2D underwater explosion problem. (f) Computed density, velocity, pressure contours at $t = 0.5488E − 04$ s for 2D underwater explosion problem. (g) Computational meshes at $t = 0$ s and $t = 0.5488E − 04$ s for 2D underwater explosion problem (npoin $= 60,121$, nelem $= 119,286$). (h) Computed $X$-component, and $Y$-component mesh velocity at $t = 0.5488E − 04$ s for 2D underwater explosion problem. (i) Computed bubble shape at different time for 2D underwater explosion problem.
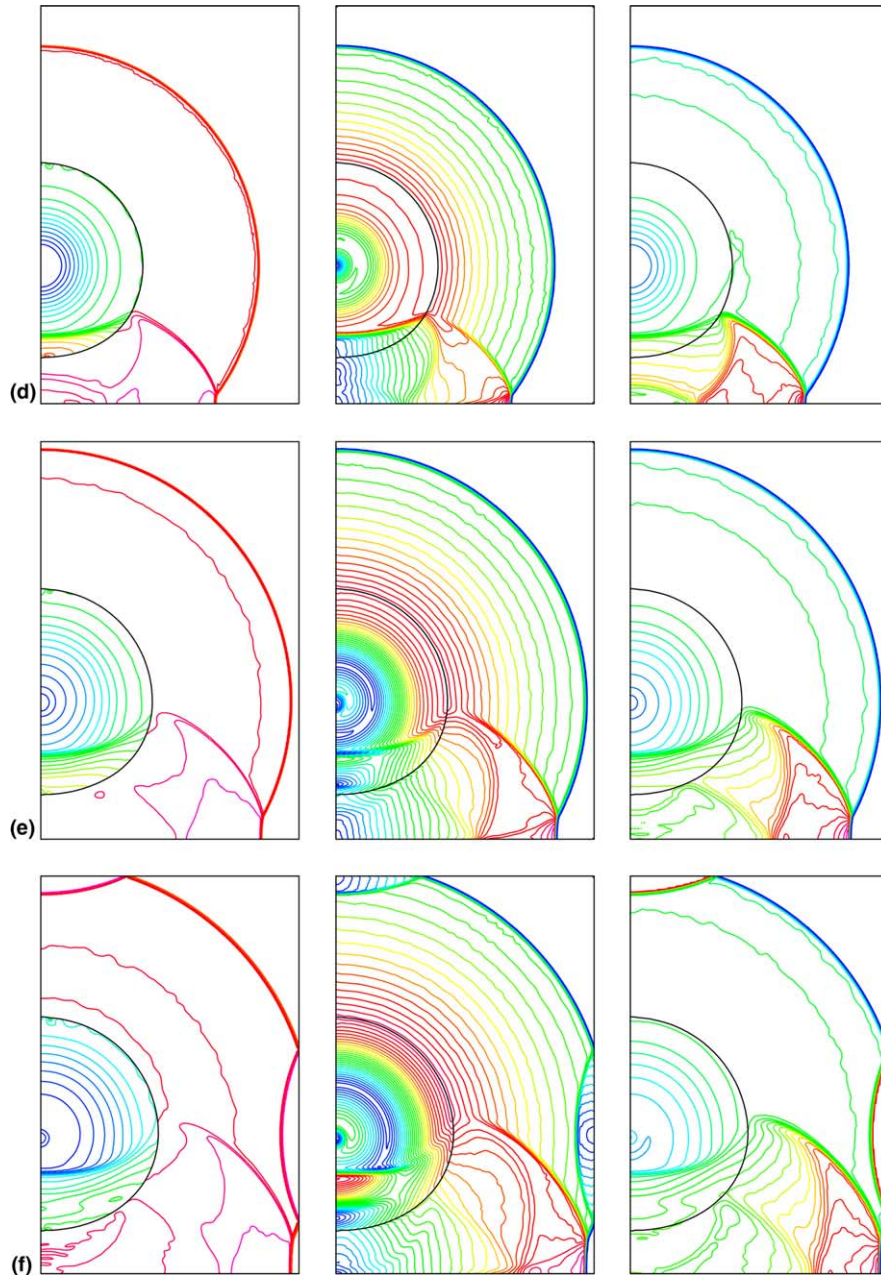
Fig. 7. (*continued*)

the bubble. The reflected rarefraction wave then hits the bottom of the tank, and the resulting reflected wave is then moving toward the water/bubble interface at a reduced shock strength (Fig. 7(d)). At later time, the primary shock wave hits both top and side of the tank (Fig. 7(e)) .This results in two reflected shock waves from top and bottom (Fig. 7(f)). Note that the present ALE HLLC method preserves very well the water/gas material interface and no spurious oscillations are produced during the computation, clearly
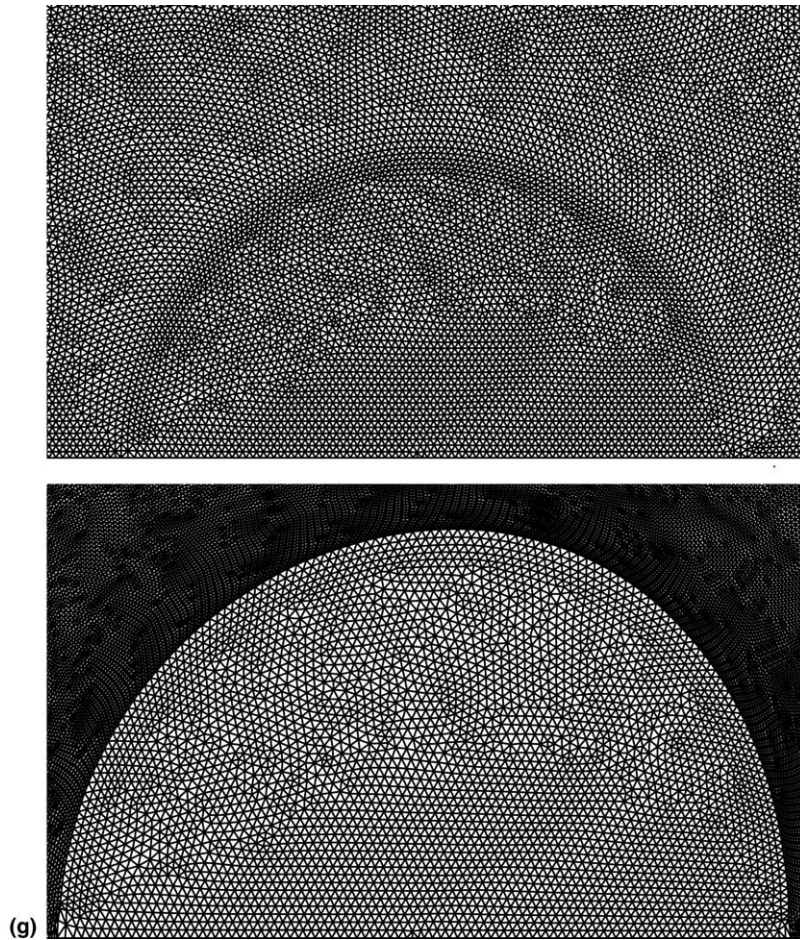
Fig. 7. (*continued*)

demonstrating the potential of the purposed ALE method for the simulation of underwater explosion problems.

## 6. Conclusions

AUSM+, HLLC, and Godunov schemes have been presented and implemented in the context of ALE formulation. The developed methods have been used for computing a variety of multi-material interface problems, where the material interface is explicitly tracked as a Lagrangian surface in an effort to ensure the unambiguous separation of different phases during the computation. Computational results show that even first order ALE AUSM+ scheme fails to yield a monotonic solution and leads to the collapse of calculation for the underwater explosion problem. Despite its simplicity, ALE AUSM+ scheme should not be considered suitable and appropriate for this class of problems. On the other hand, both ALE HLLC and Godunov schemes are found to be able to offer accurate and robust solutions for capturing strong shock, contact, and phase discontinuities on arbitrarily moving grids.
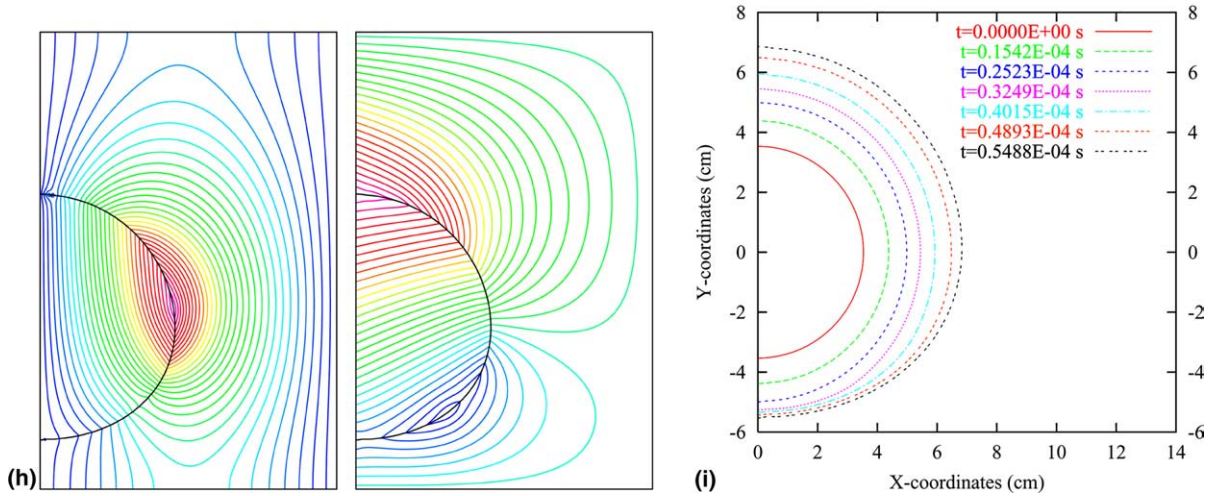
Fig. 7. (*continued*)

The preliminary results for 2D examples confirm that both ALE HLLC and Godunov methods are able to preserve excellent material interface resolution without generating any spurious oscillations in the vicinity of discontinuities for higher dimension problems. This makes ALE methods especially attractive for many applications where the material interfaces are not subjected to large deformation and complicated phenomena near the interfaces require material interface tracking in order to obtain accurate results. Ongoing work on automatic restructuring and remeshing will help to extend the current method to more complex interface problems, where large interface deformation will unavoidably lead to significant distortion of the mesh. It is our expectation that the present ALE methods combined with automatic restructuring and remeshing offered by unstructured grids will ultimately provide an accurate, robust, and viable algorithm for computing complex interface problems.

## Acknowledgements

## References

[1] R.W. Smith, A geometrically conservative arbitrary Lagrangian–Eulerian flux splitting scheme, Journal of Computational Physics 150 (1999) 268–286.
[2] A.B. Wardlaw, H. Mair, Spherical solutions of an underwater explosion bubble, Shock and Vibration 5 (1998) 89–102.
[3] R.J. LeVeque, K.M. Shyue, Two-dimensional front tracking based on high resolution wave propagation methods, Journal of Computational Physics 123 (1996) 354–368.

[4] J. Falcovitz, A. Birman, A singularities tracking conservation law for compressible duct flows, Journal of Computational Physics 115 (1994) 431–439.

[5] K.M. Shyue, An efficient shock-capturing algorithm for compressible multicomponent problems, Journal of Computational Physics 142 (1998) 208–242.

[6] Y.Y. Niu, Simple conservative flux splitting for multicomponent flow calculations part B, Numerical Heat Transfer 38 (2000) 208–242.

[7] S. Karni, Multi-component flow calculations by a consistent primitive algorithm, Journal of Computational Physics 112 (1994) 31–43.

[8] R. Abgrall, How to prevent pressure oscillations in multi-component flow calculations: a quasi-conservative approach, Journal of Computational Physics 125 (1996) 150–162.

[9] H. Luo, J.D. Baum, R. Löhner, A hybrid interface capturing method for compressible multi-fluid flows on unstructured grids, AIAA 96-0416 (1996).

[10] M.S. Liou, Progress towards an improved CFD method: AUSM+, Journal of Computational Physics 129 (1996) 364–382.

[11] P. Batten, M.A. Leschziner, U.C. Goldberg, Average-state Jacobians and implicit methods for compressible viscous and turbulent flows, Journal of Computational Physics 137 (1997) 38–78.

[12] P. Colella, H.M. Glaz, Multifluid algorithm for Eulerian finite difference methods, Private Communication.

[13] H. Zhang, M. Reggio, J.Y. Trépanier, R. Camaero, Discrete Form of the GCL for moving meshes and its implementation in CFD schemes, Computers & Fluids 22 (1993) 9.

[14] B. Nkonga, H. Guillard, Godunov-type method on non-structured meshes for three-dimensional moving boundary problems, Computer Methods in Applied Mechanics and Engineering 113 (1994) 183.

[15] M. Lesoinne, C. Farhat, Geometric conservation laws for flow problems with moving boundaries and deformable meshes, and their impact of aeroelastic computations, Computer Methods in Applied Mechanics and Engineering 134 (1996) 71.

[16] P.L. Roe, Approximate Riemann solvers, parameter vectors, and difference schemes, Journal of Computational Physics 43 (1981) 357–372.

[17] B. van Leer, Flux vector splitting for the Euler equations, Lecture Notes Physics 170 (1982) 507.

[18] H. Luo, J.D. Baum, R. Löhner, An accurate, fast, matrix-free implicit method for computing unsteady flows on unstructured grids, Computers & Fluids 30 (2001) 137–159.

[19] B. van Leer, Towards the ultimate conservative difference scheme. II. Monotonicity and conservation combined in a second order scheme, Journal of Computational Physics 14 (1974) 361–370.

[20] E. Swift, J. Decius, Measurement of Bubble Pulse Phenomena, Navord Report, 1946.

[21] C. Mader, Numerical Modeling of Detonation, University of California Press, Los Angeles, CA, 1979.

[22] C.W. Hirt, B.D. Nichols, Volume of fluid (VOF) method for the dynamics of free boundaries, Journal of Computational Physics 39 (1981) 201–225.

[23] W. Mulder, S. Osher, J. Sethian, Computing interface motion in compressible gas dynamics, Journal of Computational Physics 100 (1992) 209–228.

[24] R.K. Fedkiw, T. Aslam, B. Merriman, S. Osher, A non-oscillatory Eulerian approach to interfaces in multimaterial flows (the ghost fluid method), Journal of Computational Physics 152 (1999) 457–492.

[25] J. Glimm, J.W. Grove, X.L. Li, D.C. Tan, Robust computational algorithms for dynamic interface tracking in three dimensions, SIAM Journal on Scientific Computing 21 (2000) 2240–2256.

[26] G.J. Ball, A free-Lagrange method for unsteady compressible flow: simulation of a confined cylindrical blast wave, Shock Wave 5 (1996) 311–325.

[27] G.D. Van Albada, B. van Leer, W.W. Roberts, A comparative study of computational methods in cosmic gas dynamics, Astronomy and Astrophysics 108 (1982) 76–84.